Advanced Materials

ADVANCED MATERIALS
www.advmat.de

RESEARCH ARTICLE OPEN ACCESS

Electric-Current-Assisted Nucleation of Zero-Field Hopfion Rings

Xiaowen Chen[1,2] | Dongsheng Song[3,4] | Filipp N. Rybakov[5] | Nikolai S. Kiselev[6] | Long Li[4,7] | Wen Shi[2] | Rui Wu[1] | Xuewen Fu[8,9] | Olle Eriksson[5,10] | Stefan Blügel[6] | Rafal E. Dunin-Borkowski[11] | Haifeng Du[3,4] | Fengshan Zheng[1,2]

[1]Spin-X Institute, School of Physics and Optoelectronics, State Key Laboratory of Luminescent Materials and Devices, Guangdong-Hong Kong-Macao Joint Laboratory of Optoelectronic and Magnetic Functional Materials, South China University of Technology, Guangzhou, China | [2]Center for Electron Microscopy, South China University of Technology, Guangzhou, China | [3]Information Materials and Intelligent Sensing Laboratory of Anhui Province, Institutes of Physical Science and Information Technology, Anhui University, Hefei, China | [4]Anhui Province Key Laboratory of Low-Energy Quantum Materials and Devices, High Magnetic Field Laboratory, HFIPS, Chinese Academy of Sciences, Hefei, China | [5]Department of Physics and Astronomy, Uppsala University, Uppsala, Sweden | [6]Peter Grünberg Institute, Forschungszentrum Jülich and JARA, Jülich, Germany | [7]University of Science and Technology of China, Hefei, China | [8]Ultrafast Electron Microscopy Laboratory, The MOE Key Laboratory of Weak-Light Nonlinear Photonics, School of Physics, Nankai University, Tianjin, China | [9]School of Materials Science and Engineering, Smart Sensing Interdisciplinary Science Center, Nankai University, Tianjin, China | [10]Wallenberg Initiative Materials Science for Sustainability, Uppsala University, Uppsala, Sweden | [11]Ernst Ruska-Centre for Microscopy and Spectroscopy with Electrons, Forschungszentrum Jülich, Jülich, Germany

Correspondence: Filipp N. Rybakov (philipp.rybakov@physics.uu.se) | Nikolai S. Kiselev (n.kiselev@fz-juelich.de) | Fengshan Zheng (zhengfs@scut.edu.cn)

Received: 24 November 2025 | **Revised:** 11 February 2026 | **Accepted:** 2 March 2026

Keywords: homotopy group | hopfions | lorentz transmission electron microscopy | micromagnetic simulation | skyrmions

ABSTRACT

Magnetic hopfions are 3D topological solitons – knotted, vortex-like spin configurations. In chiral magnets, hopfions can appear as isolated structures or they can be linked to skyrmion strings. Previous studies employed a sophisticated protocol and a special sample geometry to nucleate such hopfions linked to one or a few skyrmion strings. Here, we introduce an electric-current-assisted nucleation protocol that is simple and independent of the sample shape and size. The resulting hopfions exhibit extraordinary stability in the presence of both positive and negative magnetic fields, in perfect agreement with micromagnetic simulations. We also present a comprehensive framework for classifying hopfions, skyrmions, and merons by deriving the corresponding homotopy group.

1 | Introduction

Topological magnetic solitons are localized, particle-like magnetization textures [1] that are characterized by well-defined sizes, positions, and velocities. Their motion and interactions can be controlled by external stimuli like magnetic fields, temperature, or electric currents. This makes topological magnetic solitons highly promising for future applications [2–4].

Chiral magnets represent a unique class of crystals in which a wide variety of 2D and 3D topological solitons can coexist. Skyrmions are a representative example of 2D topological solitons. In bulk crystals, skyrmions appear as string-like filamentary textures that penetrate the entire sample, but are essentially localized only in the 2D plane perpendicular to the string. Purely 3D topological solitons, commonly referred to as hopfions, are magnetic textures that are well localized in all three spatial

dimensions and, unlike skyrmions, can move freely in any spatial direction.

Topological solitons in classical field theory share some similarities with particles in quantum field theory. In particular, they are characterized by topological invariants that, to an extent, play the role of conserved quantum numbers – quantities that remain unchanged even when solitons combine, interact or even merge. Remarkably, the topological invariants of solitons, together with their addition operation, define a homotopy group. In particular, the homotopy group of 3D topological solitons is closely related to Hopf's fundamental result on nontrivial mapping from the 3-sphere to the 2-sphere. This connection gives rise to the term *hopfion*, whose meaning varies throughout the literature and is also applied to phenomena that are beyond the scope of this work [5–10].

Currently, two classes of systems are known to host statically-stable magnetic hopfions: crystals with frustrated (competing) exchange interactions [11–15] and chiral magnetic crystals. The latter is currently the only type of magnet where hopfions have been experimentally observed. These observations include hopfion rings linked to skyrmion strings [16] and, more recently, isolated objects [17, 18], which are usually referred to as *helikknotons* [19, 20].

In the previous study, the protocol for hopfion ring nucleation in the transmission electron microscope (TEM) was technically sophisticated. In particular, it required *in situ* monitoring of the magnetization texture across the entire sample, including the sample edges, as well as fine adjustment of the applied magnetic field based on the observed Lorentz TEM contrast. Such an intricate approach depends on the shape, size, and quality of the sample and presents significant obstacles to the experimental study and practical applications of magnetic hopfions.

Here, we demonstrate that magnetic hopfions linked to skyrmion strings can be nucleated more efficiently using electric currents. The experimental setup used in this study is similar to that utilized for the electric current generation of isolated hopfions in ref. [17]. Building upon this approach, we report the remarkable stability of magnetic hopfion rings under both positive and negative applied magnetic fields and demonstrate excellent agreement between experimental phenomena and micromagnetic simulations. Furthermore, we present an in-depth homotopy group analysis that provides a comprehensive framework for classifying coexisting magnetic solitons (merons, skyrmions, and hopfions) in a background of helical modulations.

2 | Experimental Setup

An electron-transparent sample for our experiment was fabricated from a single B20-type FeGe crystal using the focused ion beam (FIB) milling technique [21]. The two ends of the sample were connected to thick Pt electrodes (Figure 1a). The sample has lateral dimensions of 5.5 μm × 3.4 μm and a thickness of approximately 170 nm. The thickness of the sample in the electrode connection regions is significantly greater (Figure 1b). A similar experimental setup was used earlier [21, 22]. Further details about the experimental setup and sample preparation are available in the Methods section. An electric current pulse with a duration of 20 ns and a tunable voltage amplitude was applied to the sample. The current density, J, was estimated to be $(9.3 \pm 0.2) \times 10^{10}$ A/m^2. The experiment was carried out at a sample temperature of ∼ 95 K.

3 | Current-Assisted Nucleation of Hopfions

Figure 1c shows a representative magnetic state after applying current pulses in zero magnetic field. Before applying the current, the sample was saturated by a strong positive perpendicular magnetic field. (See Video S1 for sequential switching of the magnetic state under 1 Hz electric current pulses). Based on previous studies, the appearance of a cluster of skyrmions and helical spirals results from Joule heating induced by the electric current [23–25]. While other effects, such as spin-transfer torque and Oersted fields, may also contribute, they are not expected to play a leading role here. For the pulse conditions used in this work, the Oersted field can be estimated as $\mu_0 H_{\mathrm{Oe}} \sim 10$ mT, based on the applied current density and sample geometry. This value is approximately an order of magnitude smaller than the effective dipolar and applied magnetic fields relevant for the observed magnetic configurations. Similarly, the influence of the spin-transfer torque on the nucleation/annihilation of magnetic textures at the given current density is several times smaller than the effect of Joule heating, as estimated in ref. [26]. These order-of-magnitude considerations support the conclusion that Joule heating provides the dominant driving mechanism. The nucleation of hopfion rings is a stochastic process. In this work, we estimate a probability of approximately 10% for the formation of hopfion rings at a pulse current density of 9.3×10^{10} A/m^2.

The absence of magnetic contrast around the cluster in Figure 1c,d suggests that most of the sample volume is occupied by helical or conical modulations with a **k**-vector perpendicular to the plate. In zero magnetic field, the ground state of the FeGe thin film is a helical spiral with a **k**-vector in the plane of the film [27, 28], whereas phases with other **k**-vectors appear as metastable states. This effect becomes pronounced in extended plates and at low sample temperatures.

In order to isolate magnetic hopfion rings from the current-induced clusters, we applied an external magnetic field perpendicular to the plate. Representative examples of magnetic-field-driven nucleation of the hopfion ring are shown in Figure 2. Each row shows a distinct experimental series of four stages arranged in four columns. The first column shows initial skyrmion clusters in zero applied magnetic field after applying an electric current pulse. After cluster nucleation, we applied a magnetic field in the negative direction, i.e., opposite to the direction of the magnetic field that was initially applied to saturate the sample. In an opposite magnetic field of ∼ 230 − 280 mT (see the middle column of Figure 2), most of the skyrmions in the cluster collapse and only configurations with typical hopfion ring contrast remain stable. We then reduced the applied magnetic field to zero, inverted its direction and increased the field in the positive direction. Remarkably, the sequential application of a moderate magnetic field in the positive and negative directions, or switching the field off, did not result in instability of the hopfion rings (see, e.g., Figure 3e and Figures S1 and S2).

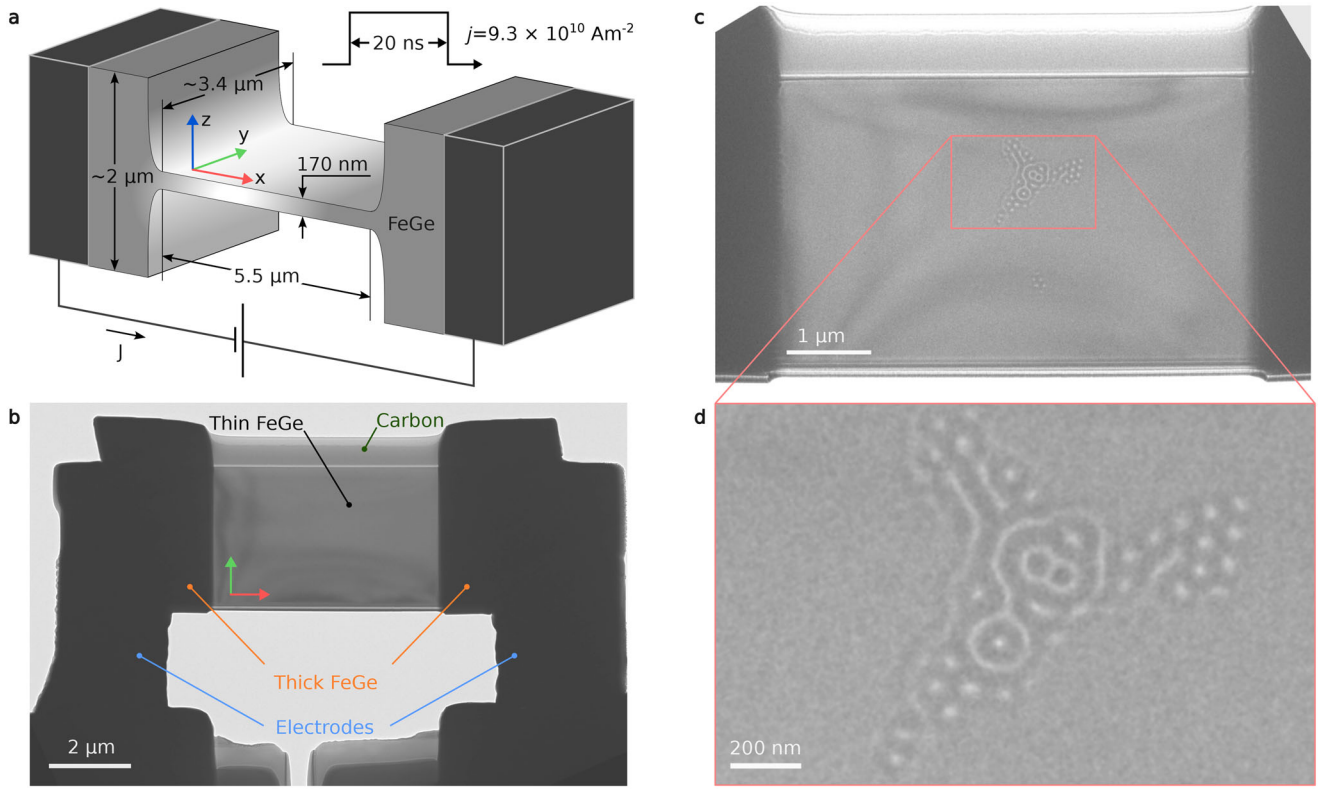

FIGURE 1 | Setup for electric-current-assisted experiments in the transmission electron microscope. a) Schematic representation of an FeGe sample. b) Low-magnification TEM image of the device viewed along the $+z$ direction. Electrodes were connected to the thicker edges of the sample. An amorphous, non-conductive carbon layer was deposited on one side of the sample during fabrication with focused ion beam (FIB) milling. c) Over-focus Lorentz TEM image of a representative magnetic state that appears after a short current pulse. The image is taken at a defocus distance of 700 µm and a temperature of 95 K. d) Magnified view of the area in (c), showing a cluster of magnetic skyrmions and other magnetic textures.

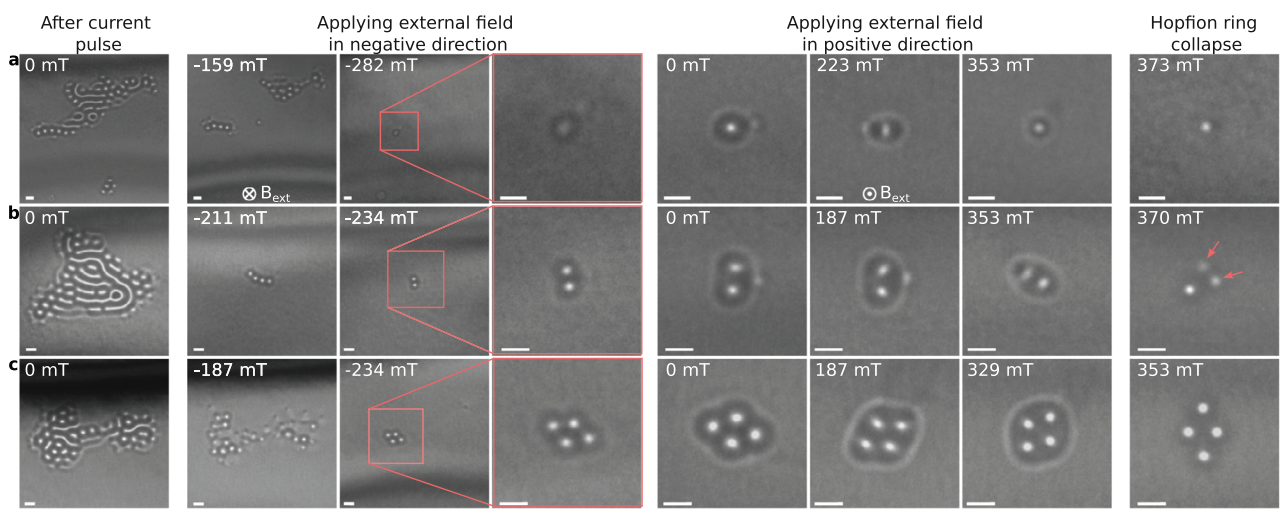

FIGURE 2 | Magnetic hopfion ring nucleation. Each row represents a distinct sequence of over-focus Lorentz TEM images, illustrating the protocol for the nucleation of magnetic hopfion rings around (a) one, (b) two and (c) four magnetic skyrmion strings. The first column shows the initial configuration obtained after applying a short electric current pulse in zero magnetic field. The second and third columns illustrate the evolution of the contrast under an external magnetic field applied in the negative direction (opposite to the initial direction of the saturating field). This step is required to collapse large skyrmion clusters and to obtain an isolated hopfion ring. The fourth column provides a magnified view of the images in the third column. The fifth to seventh columns show the evolution of Lorentz TEM contrast of hopfion rings as the applied field is increased in the positive direction. The rightmost column displays the contrast immediately after the hopfion ring collapses. The arrows in (b) mark the positions of low-intensity spots corresponding to chiral bobbers or dipolar strings (torons). The images were recorded at a defocus distance of 700 µm and a temperature of 95 K. The scale bar in all images corresponds to 100 nm.

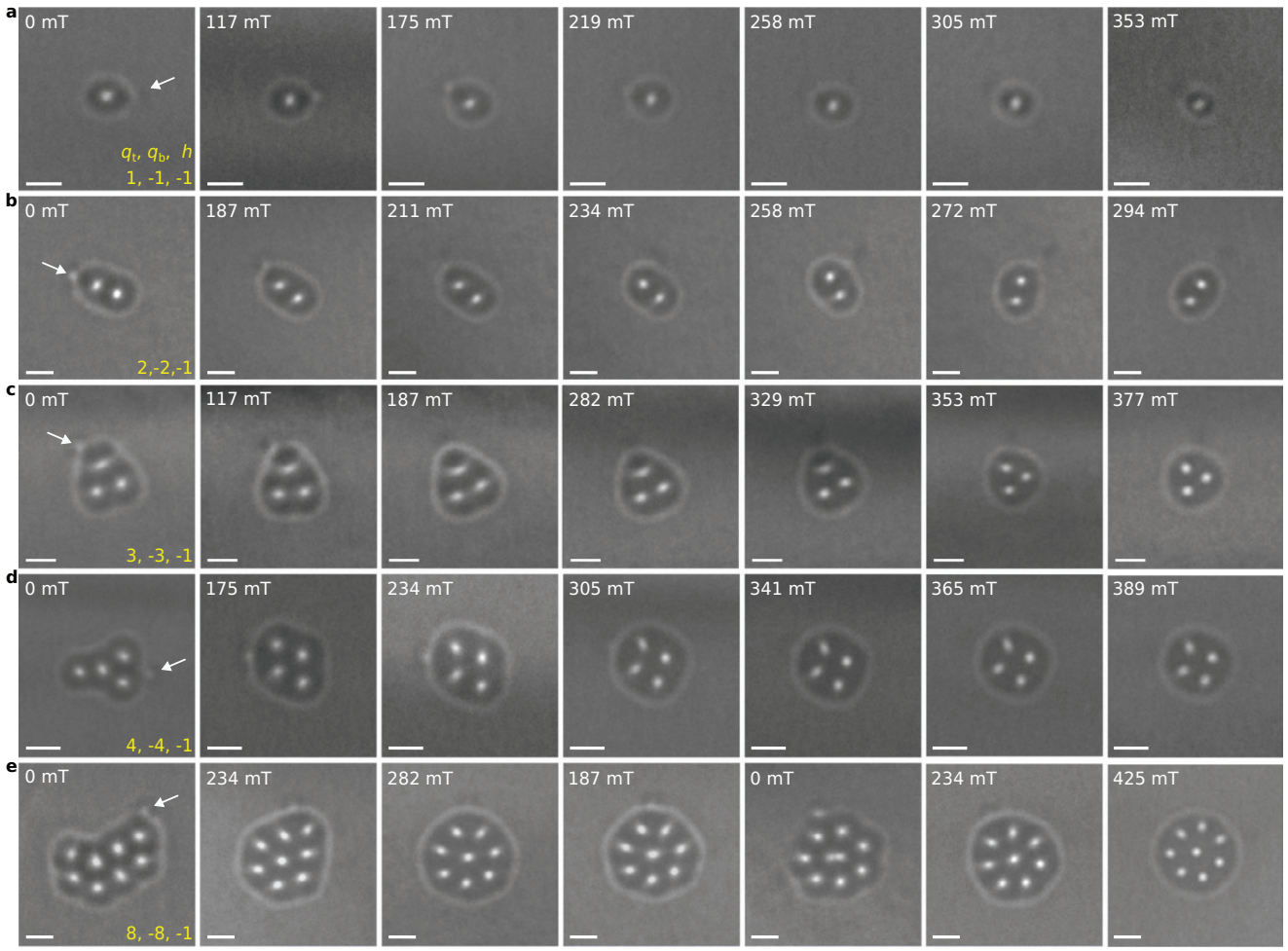

FIGURE 3 | Magnetic-field-driven evolution of hopfion rings. Each row shows a sequence of over-focus Lorentz TEM images recorded between zero magnetic field and the field at which the hopfion ring collapses. The strength of the magnetic field is labeled in the upper left corner of each image. In a–d), the magnetic field increases from left to right. In e), the magnetic field increases, decreases to zero and then increases again. The arrows in the images recorded in zero magnetic field indicate the position of a bump that is present in each hopfion ring. With increasing field, such bumps become less pronounced. All of the images were recorded at a sample temperature of 95 K and a defocus distance of 700 µm. The scale bar in all images is 100 nm. The three indices shown in the lower right corner in the first column represent the topological charges of the magnetic textures in the corresponding row: two 2D topological indices q_t and q_b and one 3D topological index h. The cone winding number is $v = 2$ for all configurations. See Figure S6 for corresponding simulated images.

As illustrated in the last column of Figure 2, the hopfion rings collapse only when the magnetic field approaches ~ 350 – 370 mT. In some cases, collapse of the hopfion ring leads to collapse of the skyrmion strings as shown in Figure 2b. When the hopfion ring collapses, we often observe the appearance of spots with low-intensity contrast, which are associated with chiral bobbers [29] or dipole strings [30–32]. (See Figure 2b and Figure S5h). However, in most cases the hopfion rings collapse, leaving no visible contrast (see Figure 2a,c). This phenomenon was also reported earlier [16].

In order to demonstrate the efficiency of electric-current-assisted hopfion ring nucleation, Figure 3 shows a collection of hopfion rings with varying numbers of skyrmion strings and their field evolution. The images illustrate the stabilty of hopfion rings in the presence of relatively high magnetic fields, which sometimes exceed 400 mT. Figures S3 and S4 show the entire field of view corresponding to the configurations in Figure 3a,c, respectively. These results also highlight the translational and rotational mobility of a hopfion ring within the sample during field evolution. In our high-quality sample, we did not observe either the hopfion pinning effect or a predominant area of hopfion ring nucleation under the current pulses.

Increasing the applied magnetic field weakens the intensity of the hopfion rings and reduces the distance between the skyrmions, as reported in the previous study [16]. Furthermore, the skyrmion clusters become more symmetric with increasing field, while the surrounding hopfion rings become more circular. Figure S5 shows a series of additional experimental images that illustrate the field evolution of a hopfion ring enclosing three skyrmion strings. Figure S6 shows simulated Lorentz TEM images, which are in perfect agreement with the experimental images shown in Figure 3.

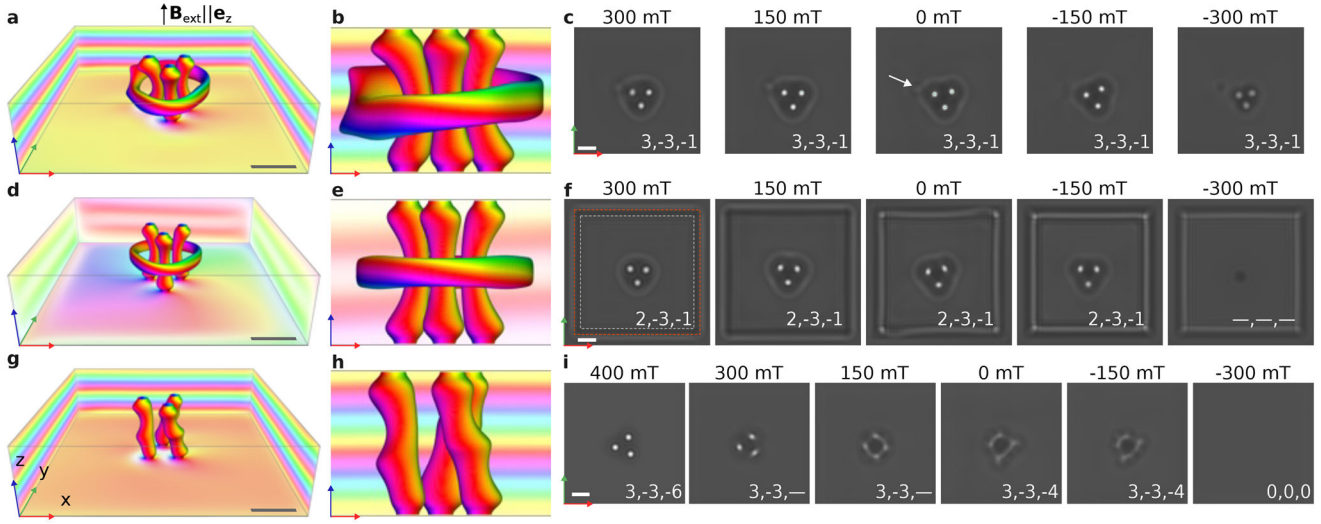

FIGURE 4 | Micromagnetic simulations for a 170-nm-thick FeGe plate. a) Hopfion surrounding the three skyrmion strings in an external magnetic field of 300 mT, obtained through micromagnetic energy minimization using parameters specific to FeGe. The calculation was performed in a 640 nm × 640 nm × 170 nm domain with periodic boundary conditions in the x-plane and a 7.5 nm damaged surface layer on the top and bottom surfaces. The magnetization is visualized by an isosurface for $m = 0$ and at the domain edges. Directions are color-coded using the standard scheme: white and black pixels indicate moments aligned parallel and antiparallel to the z-axis, while red, green and blue represent the azimuthal angle relative to the x-axis. b) Side view along the y-axis of the configuration shown in (a). c) Magnetic field evolution of the simulated over-focus Lorentz TEM contrast for the configuration shown in a) in the presence of external magnetic fields applied along the positive and negative z-axis directions. The arrow in the middle image (0 mT) marks a bump similar to that observed in the experimental images in Figures 2 and 3. The three indices in the lower right corner indicate the topological charge, which consists of two 2D topological indices q_t and q_b and one 3D topological index h. For all of the textures in this figure, the background winding number is $v = 2$. d) Stable magnetization configuration, similar to that in a), but calculated with open boundary conditions at 300 mT. e) Side view of the isosurface for $m = 0$ showing greater symmetry of the hopfion, as compared to the state shown in b). f) Simulated Lorentz TEM images similar to those in c), but for the confined geometry depicted in d). The outer (red) dashed square marks the shape of the sample. The inner (white) dashed square marks the volume in which the topological indices were calculated to avoid the impact of edge modulations. At approximately −250 mT, the edge modulations contract toward the center, leading to the collapse of the hopfion ring and skyrmions. The configuration in f) at −300 mT contains singular points, and topological indices are undefined. g) Skyrmion cluster composed of three skyrmion strings at 300 mT. h) Side view of the skyrmion cluster depicted in g). i) Simulated Lorentz TEM images of the skyrmion cluster, showing a braiding effect with decreasing applied magnetic field. At approximately −200 mT, the skyrmions in the cluster collapse. The scale bar in all images is 100 nm.

4 | Stability and Characteristic Features of Hopfion Rings

A feature that appears in most of the experimental images is a bump in each hopfion ring, which is most evident in images recorded in low applied magnetic fields (see, e.g., Figure 3, marked by white arrows). Figure S5 illustrates the varying position of the bump and the rotational degree of freedom of the hopfion ring during applied magnetic field cycles. Figure S7 contains an additional collection of images recorded in both over-focus and under-focus regimes, which show that the bumps become less visible with increasing applied magnetic field.

Micromagnetic simulations were performed to explain the origin of the bumps. (See the Methods section for details). Figure 4a shows the equilibrium configuration of a hopfion ring surrounding three skyrmion strings. Simulations were performed with periodic boundary conditions in the xy-plane to mimic the extended plate. The configuration is embedded in a regular conical phase, which distorts the toroidal shape of the hopfion ring. The distortion is visible in the side view shown in Figure 4b. The simulated Lorentz TEM images in Figure 4c show the same bumps as in the experimental images. In the case of open boundary conditions (Figure 4d), the surrounding conical phase contains a vortex (meron) with a core at the center of the domain. In this scenario, the hopfion ring appears more symmetrical (Figure 4e). The corresponding Lorentz TEM images are free of the characteristic bump (Figure 4f). The presence of the bumps can be explained by a slight distortion of the hopfion ring embedded in a regular conical phase. In particular, the step-like bending of the hopfion ring isosurface, visible in Figure 4a,b, leads to a localized deviation of the projected in-plane magnetization from the symmetric case. This deviation coincides spatially with the position of the bump observed in the corresponding Lorentz TEM images. The presence or absence of this feature in Lorentz TEM contrast, therefore, depends on the lateral size of the sample.

The images in Figure 4c,f also show that the sizes of the hopfion rings and the magnetic field range for their existence in the extended film and the sample of finite size are different. Demagnetizing field effects and the presence of edge modulations result in hopfion ring collapse in a sample of finite size at negative fields. In the case of an extended film, the hopfion ring remains stable in the range from +300 to −300 mT (Figure 4c). In contrast, the hopfion ring collapses at about −250 mT in the confined sample

(Figure 4f). The edge modulations contract toward the center of the sample, leading to the collapse of the hopfion ring and skyrmions and the appearance of a state containing Bloch points. Similar configurations have been considered in Refs. [30, 32, 33], see also the final image in Figure 4f and Figure S8j,l. Contraction of the edge modulations, leading to collapse of the internal configurations, explains why stability of the hopfion rings up to strong negative fields was not observed in the previous study [16], in which a relatively small square-sized sample ($\sim 1\,\mu m \times 1\,\mu m$) was studied.

The protocol presented above and micromagnetic simulations (Figure 4d–f) suggest that skyrmions linked to hopfions exhibit stability in a wide range of positive and negative magnetic fields. In contrast, clusters of isolated skyrmions exhibit much weaker stability in negative fields. The results of the micromagnetic simulations are in perfect agreement with the experimental observations. Figure 4g–i illustrates the behavior of a standalone cluster of three skyrmions in positive and negative perpendicular magnetic fields. Skyrmions form almost straight strings in a strong positive field of 400 mT. As the field is decreased, the skyrmion cluster transforms into skyrmion braids. The latter behavior is evident from the characteristic blurry contrast of skyrmion strings in Lorentz TEM images [34]. The skyrmion braids remain stable in zero field and survive in moderately negative fields. However, at approximately −200 mT, all of the skyrmions in the cluster collapse. An isolated skyrmion exhibits similar behavior in negative fields [35]. Thus, skyrmions inside hopfion ring are more stable against negative magnetic fields than isolated skyrmions (compare Figure 4c,i). The surrounding hopfion ring suppresses the expansion of the skyrmion core and prevents its transformation into a helical spiral state, thereby extending the stability range of the enclosed skyrmions under negative magnetic fields.

In addition to the shape and size of the sample, an essential factor underlying the phenomena presented here is the presence of a damaged layer on the surface of the sample, resulting from sample preparation using the FIB milling technique [31, 36]. Previous studies have shown that this FIB-damaged layer can be approximated as amorphous FeGe, which exhibits the same magnetization and exchange stiffness as B20-type FeGe, but has negligibly weak DMI [16, 31]. Figure S9 highlights the important role of the damaged layer by comparing the field evolution of a hopfion ring in systems with and without it.

It is important to emphasize that neither the sample shape nor the presence of the FIB-damaged surface layer is responsible for stabilizing hopfion rings. The stability of hopfion rings is governed primarily by the competition between the isotropic Heisenberg exchange and the bulk-type DMI. Hopfion rings studied here occur in a helical magnetic background with zero net magnetization. As a result, their lowest-energy configuration is realized at zero applied magnetic field, and any external magnetic field increases their energy, leading to a shrinking and eventual collapse of the hopfion rings. This behavior differs qualitatively from hopfions stabilized in chiral magnets but embedded in a field-polarized ferromagnetic background, where stability is achieved through geometrical confinement and specially imposed boundary conditions, as discussed in Refs. [5–7, 37, 38].

5 | Homotopy Group Analysis

The stability of hopfion rings in an invertible magnetic field raises an important question concerning the topological classification of such magnetic configurations. In a previous study [16], we demonstrated that hopfion rings can be classified using the skyrmion–hopfion topological charge, represented as an ordered pair of integers. This classification applies to magnetic configurations in a sufficiently polarized background. An example is the conical phase with a **k**-vector directed along the field. In this scenario, the magnetization vectors of the conical phase form a circle on the $\mathbb{S}^2$ sphere, which can always be contracted continuously to a single point $\mathbf{m}_0$, the closest equidistant point to any point on that circle. However, in the present experiment, the background phases are not necessarily field-polarized. In particular, in zero magnetic field the conical phase transforms into a helical phase, which forms a circle corresponding to the equator of the $\mathbb{S}^2$ sphere. Such a state has no net magnetization. In this case, the classification approach proposed in ref. [16] becomes ambiguous due to the absence of a well-defined polarity. In order to generalize the classification of topological magnetic textures, we considered an additional limiting case, in which the vacuum is treated as noncontractible to a single point on the spin sphere. (See details of the homotopy analysis and the derivation of the corresponding group in the Methods section). Here, we focus on the practical implications, which are now discussed in detail.

In order to calculate the topological charge of the configuration embedded in the cone phase or helix, we use an auxiliary map, as illustrated in Figure 5. We refer to this map, which was introduced in ref. [39], as the *dumbbell* map, as a result of the shape of the target space, which consists of two spheres that are connected by a segment (handle). Figure 5 illustrates the application of the dumbbell map to a representative magnetic configuration of a hopfion ring on a single skyrmion string embedded in a helix, with the **k**-vector parallel to the z-axis. Figure 5a,b illustrates the same magnetic configurations obtained by micromagnetic energy minimization in zero magnetic field in a domain with periodic boundary conditions in all directions. (See the Methods section). In Figure 5a, the magnetic texture is visualized in the form of an $m_z = 0.5$ isosurface, while in Figure 5b an $m_z = -0.5$ isosurface is shown for the same configuration.

Application of the dumbbell map depicted schematically in Figure 5c results in two auxiliary spin configurations, which are referred to as the top projection and the bottom projection, as shown in Figure 5d,e, respectively. The map ensures that both configurations are embedded in a ferromagnetic background with $\mathbf{m}_0 = (0, 0, -1)$ for the top projection and $\mathbf{m}_0 = (0, 0, +1)$ for the bottom projection. For each of the two projections, one can compute the 2D topological indices q_t and q_b and the 3D topological indices h_t and h_b, where "t" and "b" refer to the top and bottom projections. (See the Methods section for details). Our analysis reveals that, among the four indices, only three are linearly independent. Consequently, the corresponding topological invariants are represented by an ordered triple of

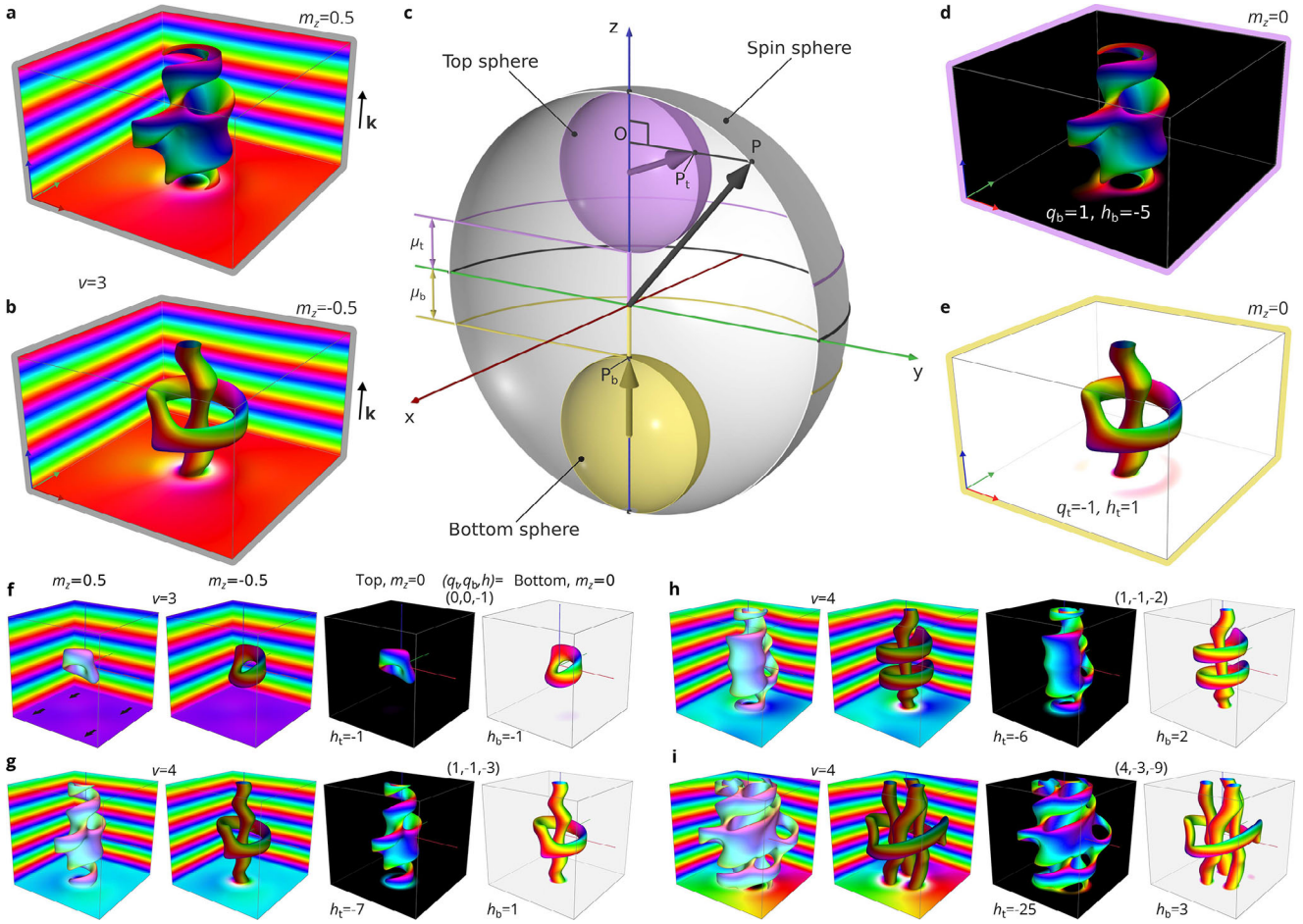

FIGURE 5 | Dumbbell map transformation for magnetic textures with topological index ($q_t = -1, q_b = 1, h = -2$). a,b) Visualizations of magnetization textures obtained by energy minimization in a domain of $5L_D \times 5L_D \times 3L_D$ with parameters for FeGe (see the Methods section for details), periodic boundary conditions in all three directions and isosurfaces of $m_z = 0.5$ and $m_z = -0.5$, respectively. The winding number $\upsilon = 3$ indicates the number of helical modulations along the z-axis. c) Dumbbell projection from the spin sphere onto a dumbbell composed of top and bottom spheres connected by a handle segment. The map is parameterized by the shape parameters μ_t, μ_b and the middle plane position between the spheres $\mu_0 = \cos\Theta_c$. The black arrow represents an example of a spin being projected. Its projections onto the top and bottom spheres are shown as magenta and yellow arrows, respectively. Video S2 illustrates this mapping for varying parameters μ_t, μ_b and μ_0. d,e) Vector fields corresponding to the normalized projection into the top and bottom spheres, respectively. The indices q_t and q_b denote the 2D topological index for the top and bottom projections. Similarly, h_t and h_b indicate the 3D topological index for the corresponding textures. f–i) Collection of topological magnetic textures with different topological index (q_t, q_b, h), where $h = h_t + \upsilon q_t = h_b + \upsilon q_b$. Each image depicts a statically stable magnetic configuration, obtained by energy minimization of the micromagnetic functional with FeGe parameters at zero magnetic field under periodic boundary conditions (Methods). Each image consists of four panels in a single row. Each panel visualizes the magnetization at the edges and the specific vector field isosurface. The first and second panels show isosurfaces for $m_z = 0.5$ and $m_z = -0.5$, respectively. The third and fourth panels show projections of magnetization on the top and bottom spheres of the dumbbell, respectively. The winding number υ between the first and second column indicates the number of helical modulations along the z-axis. The triplet of indices (q_t, q_b, h) between the third and fourth panels represents the topological charge of the corresponding configuration. f) Isolated hopfions embedded into a helix (heliknoton). g) Hopfion ring configuration, similar to the state shown in panels a) and b), but with a winding number, $\upsilon = 4$. h) Double hopfion rings on a single skyrmion string. i) Single hopfion ring on a skyrmion braid composed of three strings.

integers (q_t, q_b, h) and form a homotopy group that is isomorphic to $\mathbb{Z}^3$. (See the Methods section for details). Configurations with identical topological charges – identical tuples of topological indices – are topologically equivalent. Such an equivalence is meaningful only for configurations that are embedded in identical vacuums, meaning that they share the same magnetization background. In this study, we focus on magnetic textures that are embedded in a phase with modulations along the z-axis. The diversity of magnetic configurations embedded in such helical or conical backgrounds can be considered as classes indexed by υ – the number of periods along the z-axis. It means that such magnetic configurations can be a distinct part of a larger, or even an infinite, texture (e.g., in the case of periodic boundary conditions). Since υ inherently represents a winding number of the vacuum state along the z-axis, the sign of υ depends on the chirality of the helical modulations. (See, e.g., Figure 5f,g and Figure S10a,b). The topological index h is related to the winding number υ and the in-plane 2D topological indices q_t and q_b as follows: $h = h_t + \upsilon\, q_t = h_b + \upsilon\, q_b$. It should be noted that none of the above indices correspond directly to the *pure* skyrmion or hopfion numbers (Q or H), as they belong to different homotopy groups and describe distinct topological properties. However, the

pure skyrmion and hopfions can be recovered if the magnetic configuration is continuously transformed into a state with a uniformly polarized background. In that case, Q and H depend on the polarity of the background magnetization (see the Methods section).

The configuration depicted in Figure 5a–e has a winding number of $\upsilon = 3$ and a topological index of $(q_t, q_b, h) = (1, -1, -2)$. Topological indices (q_t, q_b, h) are also provided for the magnetic textures shown in Figures 3 and 4. Note the difference between the q_t index in Figure 4c,f due to the different background states. The topological indices of the hopfion rings in the extended plate (Figure 4a–c) and in the confined sample (Figure 4d,e) remain fixed over the entire range of stability fields. In contrast, the h index of the free-standing skyrmion cluster (Figure 4i) varies with the strength of the applied magnetic field, indicating a topological distinction between a straight skyrmion string and a skyrmion braid. This behavior reflects the fact that the 3D topological index h is not equivalent to the hopfion number, but has a more general meaning. Other hopfion-free configurations, such as skyrmions and vortices embedded in the cone phase [33, 40, 41], naturally fit within the unified classification presented here and exhibit a non-zero h index. As indicated in Figure 4i for applied magnetic fields of 300 and 150 mT, the h index may not be well-defined at intermediate magnetic fields, when the system is in a transient state.

Other representative configurations with nontrivial topology are shown in Figure 5f–i and Figure S10. In particular, Figure 5f and Figure S10a illustrate an isolated magnetic hopfion embedded in a helix (heliknoton) [18, 20]. Note that the systems in Figure 5f and Figure S10a have opposite chiralities and opposite signs of the 3D topological index. The configurations in Figure 5g and Figure S10b show a hopfion linked to a single skyrmion string, similar to the state shown in Figure 5 but in a larger simulated domain that accommodates helical spirals with winding number $\upsilon = 4$. Note that the configurations in Figure 5g and Figure 10b also have opposite chiralities. The configurations in Figure 5h and Figure S10c illustrate different linkages between hopfions and skyrmion strings. The state depicted in Figure 5i presents one of the most complex configurations, consisting of a skyrmion braid linked to a single hopfion ring embedded in a vortex cone background. Figure 10d shows a so-called hybrid skyrmion string, as studied previously in ref. [42]. The contributions of the vacuum and the skyrmion braiding effect to the topological charge of the system are illustrated in Figures 8 and 11, respectively. The diverse set of topological configurations illustrated in Figure 5f–i, Figures S8, S10, and S11 demonstrate that the topological classification presented here provides the most comprehensive framework for classifying 2D and 3D topological magnetic solitons, including merons, skyrmions and hopfions.

6 | Conclusions

We have successfully realized the nucleation of hopfion rings in an FeGe film with large lateral dimensions without the need for geometric confinement and their efficient generation by electric currents. The successful nucleation of hopfions via energy injection from pulsed electric currents suggests that other ultrafast excitations, such as laser or field pulses, may also serve as promising approaches for hopfion generation. Our results open new pathways for studying hopfion dynamics under external stimuli and pave the way for potential applications in spintronics and unconventional computing. The hopfions that we observe are stable in zero magnetic field, facilitating future tomographic studies of such three-dimensional magnetic configurations using high-resolution transmission electron microscopy [43, 44] and X-ray microscopy [45].

7 | Methods

7.1 | Specimen Preparation

An FeGe TEM specimen, fixed on an *in situ* electrical chip, was prepared from a single crystal of B20-type FeGe using a standard lift-out method from the bulk using a focused ion beam instrument (Helios Nanolab 600i, FEI) [21].

7.2 | Electric Current Experimental Setup and TEM Magnetic Imaging

Fresnel magnetic images were recorded with a TEM instrument (Talos F200X, FEI), operated at 200 kV in Lorentz mode. A single-tilt liquid-nitrogen specimen holder (Model 616.6 cryotransfer holder, Gatan) was used in a temperature range of 95 to 300 K. The experiments described in the main text were all performed at 95 K. The perpendicular magnetic field was controlled by adjusting the current of the objective lens. The electric current pulses were supplied by a voltage source (AVR-E3-B-PN-AC22, Avtech Electrosystems), with a pulse width of 20 ns and a frequency of 1 Hz [22]. The applied voltage amplitude was tunable and set to 43.5 V in the experiment. The device resistance at 95 K was approximately 500 Ω. The current pulses had a square waveform with pulse rise time/overshoot of 1–2 ns.

7.3 | Statistical Analysis

We determine a hopfion ring nucleation probability of about 10% as follows. The nucleation probability was determined from approximately 140–150 independent current pulses, of which 14 produced successful hopfion ring nucleation events. The measurements were performed on a single device depicted in Figure 1, at a pulse current density of 9.3×10^{10} A/m^2. The statistics were reproducible across repeated measurements.

7.4 | Micromagnetic Simulations

The micromagnetic model of isotropic chiral magnet includes four energy terms: the Heisenberg exchange, the Dzyaloshinskii–Moriya interaction (DMI), the Zeeman energy, and the demagnetizing field energy term:

$$\mathcal{E} = \int_{V_m} d\mathbf{r}\, \mathcal{A} \sum_{i=x,y,z} |\nabla m_i|^2 + \mathcal{D}\, \mathbf{m} \cdot (\nabla \times \mathbf{m}) - M_s\, \mathbf{m} \cdot \mathbf{B} + \\ + \frac{1}{2\mu_0} \int_{\mathbb{R}^3} d\mathbf{r} \sum_{i=x,y,z} |\nabla A_{d,i}|^2 , \quad (1)$$

where $\mathbf{m}(\mathbf{r}) = \mathbf{M}(\mathbf{r})/M_s$ is a unit vector field that defines the direction of magnetization, $M_s = |\mathbf{M}(\mathbf{r})|$ is the saturation magnetization, $\mathbf{B} = \mathbf{B}_{ext} + \nabla\times\mathbf{A}_d$ is the total magnetic field, $\mathbf{A}_d(\mathbf{r})$ is the magnetization induced magnetic vector potential, $\mathcal{A}$ is the Heisenberg exchange stiffness constant, $\mathcal{D}$ is the constant of isotropic bulk-type DMI and μ_0 is the vacuum permeability. All simulations presented in this work were performed using FeGe material parameters that have been well tested in previous studies [16, 29, 31, 34]: $\mathcal{A} = 4.75$ pJm^{-1}, $\mathcal{D} = 0.853$ mJm^{-2} and $M_s = 384$ kAm^{-1}. For these parameters, the equilibrium period of the helical spin spiral is given by $L_D = 4\pi\mathcal{A}/\mathcal{D} = 70$ nm, and the critical field for the cone phase saturation is $B_c = B_D + \mu_0 M_s = 0.682$ T, where $B_D = \mathcal{D}/(2M_s\mathcal{A}) = 0.199$ T.

The equilibrium solutions of the Hamiltonian (1) were obtained via numerical energy minimization using the Excalibur code [46] and Mumax [47]. Theoretical Lorentz TEM images were computed following the method described in ref. [34], which is implemented in Excalibur. The FIB-damaged layer was modeled by setting $\mathcal{D} = 0$, following the approach in ref. [31]. For the simulations shown in Figure 4, we used a computational domain of $L_x = L_y = 640$ nm, $L_z = 170$ nm, with a finite-difference mesh of $256 \times 256 \times 68$ nodes. For the calculations presented in Figure 5 and Figures S8, S10, and S11, we used different domain sizes but the same mesh density, periodic boundary conditions, and neglected demagnetizing fields.

7.5 | Algebraic Topological Analysis

We classify complex magnetic textures, consisting of skyrmion/meron strings and hopfions, according to their homotopy types. Each homotopy type [48] is a class of textures that can be continuously transformed into each other and is quantified by topological invariants. When identifying topological invariants, we consider realistic boundary conditions, taking into account that magnetic textures are generally localized against the background of non-perfect magnetic phases, such as near-collinear ferromagnetic or distorted helical/conical states. To address this, we employ a specialized technique – the auxiliary dumbbell map [39], which establishes a connection to the category of pointed spaces [48, 49].

7.6 | Auxiliary Dumbbell Map

The dumbbell map is schematically illustrated in Figure 5c and Video S2 (Supporting Information). It maps every spin from the $\mathbb{S}^2$ sphere onto a space composed of two spheres (top and bottom) joined by a handle – a line segment connecting the south pole of the top sphere to the north pole of the bottom sphere. For example, in Figure 5c, the point P on the spin sphere is projected onto P_t on the top sphere. The projection is performed by dropping a perpendicular to the z-axis (see segment OP) and identifying the intersection of this perpendicular line with one of the spheres. However, some spins do not have a direct projection onto a sphere. For example, in Figure 5c, P has no direct projection onto the bottom sphere. In such cases, the projected vector fields are complemented by points at the poles of the spheres. Specifically, any spin satisfying $m_z \geq \mu_b$ is mapped to the north pole of the bottom sphere (see P_b). Similarly, any spin with $m_z \leq \mu_t$ is assigned to the south pole of the top sphere (see Video S2, Supporting Information). After projecting, the spins in the upper and lower spheres must be normalized.

The sizes of the top and bottom spheres are determined by the parameters μ_t and μ_b:

$$\mu_t = +\mathcal{F}(\rho),$$
$$\mu_b = -\mathcal{F}(\rho),$$

where ρ is the reduced distance, defined as:

$$\rho = \sqrt{\left(\frac{2r_x}{L_x}\right)^2 + \left(\frac{2r_y}{L_y}\right)^2},$$

such that $\rho = 0$ at the center of any xy-plane and $\rho = 1$ near the boundaries. Here, L_x and L_y represent the dimensions of the simulated domain along the corresponding directions, while r_x and r_y denote the coordinates of a point relative to the domain center. The function $\mathcal{F}(\rho)$ can be any continuous function satisfying: $\mathcal{F}|_{\rho=0} = 0$ and $\mathcal{F}|_{\rho\geq 1} = 1$. A suitable choice is:

$$\mathcal{F}(\rho) = \begin{cases} \rho^n & \text{if} \quad \rho < 1, \\ 1 & \text{if} \quad \rho \geq 1, \end{cases}$$

where n is a positive integer. For the textures depicted in Figure 5d,e we set $n = 4$.

The explicit equations for the dumbbell map [39] are:

$$\mathbf{m}_t = \begin{pmatrix} 2\gamma_t m_x \\ 2\gamma_t m_y \\ -1 + 2\gamma_t{}^2(1+m_z)(1-\mu_t) \end{pmatrix}, \tag{2}$$

where

$$\gamma_t = \begin{cases} \sqrt{\dfrac{m_z - \mu_t}{(1+m_z)(1-\mu_t)^2}} & \text{if} \quad \mu_t < m_z, \\ 0 \quad \text{otherwise}, \end{cases}$$

and

$$\mathbf{m}_b = \begin{pmatrix} 2\gamma_b m_x \\ 2\gamma_b m_y \\ 1 - 2\gamma_b{}^2(1-m_z)(1+\mu_b) \end{pmatrix}, \tag{3}$$

where

$$\gamma_b = \begin{cases} \sqrt{\dfrac{\mu_b - m_z}{(1-m_z)(1+\mu_b)^2}} & \text{if} \quad m_z < \mu_b, \\ 0 \quad \text{otherwise}. \end{cases}$$

7.7 | Calculation of Topological Indices

To compute the topological indices of an abstract unit vector field $\mathfrak{m}$ (which may represent $\mathbf{m}$, $\mathbf{m}_t$ or $\mathbf{m}_b$, depending on the

context), we utilize the winding number integral [50], defined as:

$$W(\mathbf{m}) = \frac{1}{2\pi}\int_{\mathbb{S}^1} d\ell\, \frac{\mathbf{m}_x\,\partial_\ell \mathbf{m}_y - \mathbf{m}_y\,\partial_\ell \mathbf{m}_x}{\mathbf{m}_x^2 + \mathbf{m}_y^2}, \tag{4}$$

along with the Kronecker integral,

$$Q(\mathbf{m}) = \frac{1}{4\pi}\int_{\mathbb{I}^2} \mathrm{d}r_1\mathrm{d}r_2\, \mathbf{F}\cdot\hat{\mathbf{e}}_{r_3}, \tag{5}$$

and the Whitehead integral:

$$H(\mathbf{m}) = -\frac{1}{16\pi^2}\int_{\mathbb{I}^2\times\mathbb{S}^1} \mathrm{d}\mathbf{r}\, \mathbf{F}\cdot[(\nabla\times)^{-1}\mathbf{F}], \tag{6}$$

where $\mathbf{F}$ represents the vector of curvature, defined as

$$\mathbf{F} \equiv \begin{pmatrix} \mathbf{m}\cdot[\partial_{r_2}\mathbf{m}\times\partial_{r_3}\mathbf{m}] \\ \mathbf{m}\cdot[\partial_{r_3}\mathbf{m}\times\partial_{r_1}\mathbf{m}] \\ \mathbf{m}\cdot[\partial_{r_1}\mathbf{m}\times\partial_{r_2}\mathbf{m}] \end{pmatrix}. \tag{7}$$

The integration domains in Equations (4)-(6) are the elements of Ω – the texture localization domain [16]. The domain Ω is homeomorphic to solid torus, $\mathbb{I}^2\times\mathbb{S}^1$. Note that the section of the torus can be chosen up to homeomorphism. In particular, the square $\mathbb{I}^2$ can be equivalently replaced by the disk $\mathbb{D}^2$. The fields $\mathbf{m}$ in the above integrals must satisfy the following boundary conditions: they must be z-periodic for Equations (4)–(6) and must take the value of the base point on the boundary for Equations (5) and (6). The Whitehead integral applicability follows from the existence of natural inclusion $\mathbb{I}^2\times\mathbb{S}^1 \hookrightarrow \mathbb{S}^3$.

The integrals in Equations (4), (5), and (6) can be directly computed when the magnetization vector field is defined analytically. For vector fields defined on discrete meshes, such as those obtained from numerical simulations, we employ simplex-based equivalents [48, 50] to compute the corresponding topological indices. Specifically, for Equations (4) and (5), we follow the approach described in Refs. [39, 51]. For Equation (6), we use the numerical integration scheme outlined in ref. [16]. In particular, to increase smoothness of the vector field along the z-axis, we add a thin transient layer composed of six additional mesh nodes (cuboids) and minimize the Dirichlet energy, $\int \mathrm{d}\mathbf{r}|\nabla\mathbf{m}|^2$, within this layer assuming periodic boundary condition along the z-axis.

7.8 | Revealing Homotopy Types and Their Groups

Our analysis is based on the following commutative diagram – similar to that proposed in ref. [39] – which relates pairs of topological spaces:

$$\begin{array}{ccc} (\Omega,\partial\Omega) & \xrightarrow{\ f\ } & (\mathbb{S}^2, X) \\ & \overset{g}{\searrow} & \downarrow p \\ & & (\mathbb{S}^2\vee\mathbb{S}^2, P_0), \end{array} \tag{8}$$

where $\partial\Omega$ is the boundary of space Ω that is homeomorphic to the surface of a solid torus ($\partial\Omega\cong\mathbb{S}^1\times\mathbb{S}^1$), $\mathbb{S}^2$ is the 2-sphere denoting the space of magnetization values, $X\subset\mathbb{S}^2$ is a connected subspace of $\mathbb{S}^2$. The symbol $\vee$ stands for the wedge sum, and P_0 is the common point of the wedge, serving as the base point. For clarity, the mathematical symbols and terms used in this section are summarized in Table 1.

Every arrow in the diagram (8) represents a continuous map, and the composition $g = p\circ f$ ensures the commutativity of the diagram. We aim to determine the homotopy types of the map f and their associated groups. Homotopy types form a group under an operation that governs the combination of topological invariants when magnetic textures merge.

First, consider the case where the space X in diagram (8) is a single point. Due to homotopy equivalence, X can also be treated as any subspace of the sphere contractible to a point, such as a spherical cap or a punctured sphere. In this scenario, the relevant homotopy types form a group, previously determined in ref. [16]:

$$G_f \cong \mathbb{Z}\times\mathbb{Z} \equiv \mathbb{Z}^2 \quad (\text{if } X \simeq \text{point}). \tag{9}$$

The classification by the group (9) applies when the magnetic background is sufficiently polarized. This includes both the saturated ferromagnetic phase and the conical phase, including cases with distortions, as detailed in ref. [16]. The bottom part of the diagram can be disregarded here as it is of little significance for this part of the analysis. However, it plays a crucial role in the case discussed below.

Next, consider a more sophisticated and distinct case in which a cone transforms into a helix. In this scenario, the space X is essentially a spherical segment or its homotopy equivalent, $X\simeq\mathbb{S}^1$. To analyze this case, we begin by examining a nontrivial mapping from the z-periodic paths along the boundary of Ω:

$$\partial\Omega \ni\ \mathbb{S}^1 \to X\ \simeq \mathbb{S}^1. \tag{10}$$

The topological invariant of the map (10) is an integer υ, representing the winding number that can be computed using Equation (4), $\upsilon = W(\mathbf{m})$. Physically, υ corresponds to the number of periods of helical modulations that fit within the z-height of the domain Ω. As a result, homotopy types for f can initially be classified into distinct classes, indexed by the integer υ. To obtain detailed information about such classes, we use the entire diagram (8). The auxiliary map p in the diagram (8) is the surjective dumbbell-like transformation introduced in ref. [39]. This transformation gives rise to the emergence of the two unit vector fields $\mathbf{m}_\mathrm{t}$ and $\mathbf{m}_\mathrm{b}$. Map g in the diagram (8) is essentially a mapping from a co-H space [49], so the corresponding to g homotopy classes form a group. This group is, in turn, straightforward to derive from the result of ref. [16]:

$$G_g \cong \pi_2(\mathbb{S}^2\vee\mathbb{S}^2)\times\pi_3(\mathbb{S}^2\vee\mathbb{S}^2) \cong \mathbb{Z}^2\times\mathbb{Z}^3 \equiv \mathbb{Z}^5. \tag{11}$$

Note that G_g is not our final target group, but rather an intermediate tool for recovering insights into the actual target group G_f. In this regard, it is important that the images of the map g corresponding to different elements of G_g possess distinct homotopy types for the map f. To reveal homotopy types in f (however, generally speaking, not necessarily all of them), we iterate over specific maps for which the induced elements in

TABLE 1 | Table of symbols and terms used in this section.

Symbol	Meaning	Ref.
$\cong$	homeomorphic (for spaces) or isomorphic (for groups)	[52, 53]
$\times$	Cartesian product (spaces) or direct product (groups)	[52, 53]
$\setminus$	set-theoretic difference	[52]
$\subset$	subset	[52]
$\vee$	wedge sum of pointed spaces	[53]
$\to$	continuous map (spaces) or homomorphism (groups)	[52, 53]
$\mapsto$	maps to	
$\hookrightarrow$	inclusion map	[52]
$x \circ y$	composition of maps in the form x(y(…))	[52]
∂X	boundary of a space X	[52]
$\pi_n(X)$	n-th homotopy group of X	[52, 53]
$\mathrm{Aut}(X)$	automorphism group of X	[54]
$\mathrm{GL}_n(\mathbb{Z})$	group of $n \times n$ integer matrices that have integer inverses	[54]
$\mathbb{S}^n$	n-dimensional sphere	[52]
$\mathbb{Z}$	group of integers under addition	[54]
$\mathbb{Z}^n$	free abelian group of rank n	[54]

group G_g will differ. As a result, we reveal the following group homomorphism taking place for every fixed υ:

$$\mathbb{Z}^3 \to \mathbb{Z}^5 \cong G_g, \tag{12}$$

$$(q_\mathrm{t}, q_\mathrm{b}, h) \mapsto (q_\mathrm{t}, q_\mathrm{b}, \underbrace{h - \upsilon\, q_\mathrm{t}}_{h_\mathrm{t}}, \underbrace{h - \upsilon\, q_\mathrm{b}}_{h_\mathrm{b}}, -\upsilon\,(q_\mathrm{t} + q_\mathrm{b})). \tag{13}$$

Accordingly, the topological invariants for f are two 2D indices [39]:

$$q_\mathrm{t} = Q(\mathbf{m}_\mathrm{t}), \tag{14}$$

$$q_\mathrm{b} = Q(\mathbf{m}_\mathrm{b}), \tag{15}$$

that can be computed using Equation (5), and one 3D index that can be computed using Equation (6) by one of the following formulas:

$$h = H(\mathbf{m}_\mathrm{t}) + \upsilon\, q_\mathrm{t}, \tag{16}$$

or

$$h = H(\mathbf{m}_\mathrm{b}) + \upsilon\, q_\mathrm{b}. \tag{17}$$

Thus, the entire diversity of topological textures embedded in a conical or helical background with υ periods can be classified using an ordered triplet of integers, (q_t, q_b, h), forming the group $\mathbb{Z}^3 \equiv \mathbb{Z} \times \mathbb{Z} \times \mathbb{Z}$ under addition. Naturally, the triple has the freedom to be transformed by the action of any matrix in the group of automorphisms, $\mathrm{Aut}(\mathbb{Z}^3) = \mathrm{GL}_3(\mathbb{Z})$.

As a final note, let us emphasize the following. From the homotopy point of view, one can continuously transform the conical (helical) phase into a uniformly polarized state. Such transformation represents a transition from $X \simeq$ circle to $X \simeq$ point. This process can equivalently be described as the space X, initially a sphere with two punctures, expanding into a sphere with a single puncture. Accordingly, the corresponding inclusions induce the polarization-dependent homomorphisms onto the group (9):

$$\mathbb{S}^2 \setminus \{\hat{\mathbf{e}}_z, -\hat{\mathbf{e}}_z\} \hookrightarrow \mathbb{S}^2 \setminus \{-\hat{\mathbf{e}}_z\}, \tag{18}$$

$$(q_\mathrm{t}, q_\mathrm{b}, h) \mapsto (q_\mathrm{b}, h - \upsilon\, q_\mathrm{b}), \tag{19}$$

and

$$\mathbb{S}^2 \setminus \{\hat{\mathbf{e}}_z, -\hat{\mathbf{e}}_z\} \hookrightarrow \mathbb{S}^2 \setminus \{\hat{\mathbf{e}}_z\}, \tag{20}$$

$$(q_\mathrm{t}, q_\mathrm{b}, h) \mapsto (q_\mathrm{t}, h - \upsilon\, q_\mathrm{t}). \tag{21}$$

Thus, Equations (19) and (21) illustrate how the most general classification presented here, Equation (13), reduces to the specific case discussed in ref. [16], where topological classification is done relative to the cone contractible to a point. In other words, these equations demonstrate a more universal approach to the topological classification and capture the scenario for transition from $X \simeq$ circle to $X \simeq$ point.

It is worth noting that alternative attempts to classify similar textures can be found in the literature [41, 55–59].

Video S1 (Supporting Information) This video shows the in situ Lorentz TEM contrast during sequential electric current pulses at a frequency of 1 Hz, resulting in abrupt switching of the magnetic state.

Video S2 (Supporting Information) Dumbbell projection from the spin sphere onto a dumbbell composed of top and bottom spheres connected by a handle segment. The map is parameterized by the shape parameters μ_t, μ_b. The black arrow represents an example of a spin being projected. Its projections onto the top and bottom spheres, defined by Equations (2) and (3), are shown as magenta and yellow arrows, respectively.

Author Contributions

F.Z. conceived the project and designed the experiments. L.L. prepared the TEM samples. X.C. and D.S. performed the experiments and data analysis under the supervision of H.D. and F.Z. N.S.K. and F.N.R. developed the theory and performed numerical simulations. F.N.R. performed homotopy-group analysis. X.C., F.Z., N.S.K. and F.N.R. prepared the manuscript. All of the authors discussed the results and contributed to the final manuscript.

Acknowledgments

X.C. and F.Z. acknowledge financial support from the National Key R&D Program of China (Grant No. 2024YFA1611100, the National Natural Science Fund for Excellent Young Scientists Fund Program (Overseas) and the General Program (Grant No. 52373226), and the Fundamental Research Funds for the Central Universities. F.Z. is grateful to the GJYC program of Guangzhou (No. 2024D01J0060), the Guangzhou Basic and Applied Basic Research Foundation (No. SL2024A04J00852), the Guangdong Provincial Quantum Science Strategic Initiative (Grant No. GDZX2401002) and the Xiaomi Young Talents Program. N.S.K. and S.B. acknowledge financial support from the Deutsche Forschungsgemeinschaft through SPP 2137 "Skyrmionics", Grant No. KI 2078/1-1 and Grant No. BL 444/16-2, respectively. F.N.R. and O.E. acknowledge support from the Swedish Research Council (Grant No. 2023-04899). R.E.D-B. is grateful for financial support from the Deutsche Forschungsgemeinschaft (Project-ID 405553726 – TRR 270). This project has received funding from the European Research Council under the European Union's Horizon 2020 Research and Innovation Programme (Grant No. 856538 - project "3D MAGiC").

Open access funding enabled and organized by Projekt DEAL.

Conflicts of Interest

The authors declare no conflict of interest.

Data Availability Statement

The data that support the findings of this study are available from the corresponding author upon reasonable request.

References

1. A. M. Kosevich, B. A. Ivanov, and A. S. Kovalev, "Magnetic Solitons," *Physics Reports* 194 (1990): 117–238.

2. A. Fert, N. Reyren, and V. Cros, "Magnetic Skyrmions: Advances in Physics and Potential Applications," *Nature Reviews Materials* 2 (2017): 17031.

3. Y. Tokura and N. Kanazawa, "Magnetic Skyrmion Materials," *Chemical Reviews* 121 (2020): 2857–2897.

4. Y. Zhou, S. Li, X. Liang, and Y. Zhou, "Topological Spin Textures: Basic Physics and Devices," *Advanced Materials* 37 (2025): 2312935.

5. Y. Liu, R. K. Lake, and J. Zang, "Binding a Hopfion in a Chiral Magnet Nanodisk," *Physical Review B* 98 (2018): 174437.

6. J.-S. B. Tai and I. I. Smalyukh, "Static Hopf Solitons and Knotted Emergent Fields in Solid-State Noncentrosymmetric Magnetic Nanostructures," *Physical Review Letters* 121 (2018): 187201.

7. P. Sutcliffe, "Hopfions in Chiral Magnets," *Journal of Physics A: Mathematical and Theoretical* 51 (2018): 375401.

8. N. Kent, N. Reynolds, D. Raftrey, et al., "Creation and Observation of Hopfions in Magnetic Multilayer Systems," *Nature Communications* 12 (2021): 1562.

9. X. Yu, Y. Liu, K. V. Iakoubovskii, et al., "Realization and Current-Driven Dynamics of Fractional Hopfions and Their Ensembles in a Helimagnet FeGe," *Advanced Materials* 35 (2023): 2210646.

10. Y. Zhang, J. Tang, Y. Wu, et al., "Stable Skyrmion Bundles at Room Temperature and Zero Magnetic Field in a Chiral Magnet," *Nature Communications* 15 (2024): 3391.

11. I. L. Bogolubsky, "Three-Dimensional Topological Solitons in the Lattice Model of a Magnet With Competing Interactions," *Physics Letters A* 126 (1988): 511.

12. P. Sutcliffe, "Skyrmion Knots in Frustrated Magnets," *Physical Review Letters* 118 (2017): 247203.

13. Y. Liu, W. Hou, X. Han, and J. Zang, "Three-Dimensional Dynamics of a Magnetic Hopfion Driven by Spin Transfer Torque," *Physical Review Letters* 124 (2020): 127204.

14. F. N. Rybakov, N. S. Kiselev, A. B. Borisov, L. Döring, C. Melcher, and S. Blügel, "Magnetic Hopfions in Solids," *APL Materials* 10 (2022): 111113.

15. Z. Zhang, K. Lin, Y. Zhang, et al., "Magnon Scattering Modulated by Omnidirectional Hopfion Motion in Antiferromagnets for Meta-Learning," *Science Advances* 9 (2023): eade7439.

16. F. Zheng, N. Kiselev, F. Rybakov, L. Yang, S. Blügel, and R. Dunin-Borkowski, "Hopfion Rings in a Cubic Chiral Magnet," *Nature* 623 (2023): 718–723.

17. L. Li, D. Song, W. Wang, et al., "Electrically Writing a Magnetic Heliknoton in a Chiral Magnet," *Nature Materials* (2026): 1–6, https://doi.org/10.1038/s41563-025-02450-0.

18. X. Chen, Y. Donghai, L. Zefang, et al., "Laser-Induced Nucleation of Magnetic Hopfions," https://doi.org/10.21203/rs.3.rs-7435743/v1.

19. J.-S. B. Tai and I. I. Smalyukh, "Three-Dimensional Crystals of Adaptive Knots," *Science*365 (2019): 1449–1453.

20. R. Voinescu, J.-S. B. Tai, and I. Smalyukh, "Hopf Solitons in Helical and Conical Backgrounds of Chiral Magnetic Solids," *Physical Review Letters*125 (2020): 057201.

21. W. Wang, D. Song, W. Wei, et al., "Electrical Manipulation of Skyrmions in a Chiral Magnet," *Nature Communications*13 (2022): 1593.

22. J. Tang, Y. Wu, W. Wang, et al., "Magnetic Skyrmion Bundles and Their Current-Driven Dynamics," *Nature Nanotechnology*16 (2021): 1086–1091.

23. X. Yu, D. Morikawa, K. Nakajima, et al., "Motion Tracking of 80-nm-Size Skyrmions Upon Directional Current Injections," *Science Advances*6 (2020): eaaz9744.

24. G. Qin, X. Zhang, R. Zhang, et al., "Dynamics of Magnetic Skyrmions Driven by a Temperature Gradient in a Chiral Magnet FeGe," *Physical Review B*106 (2022): 024415.

25. X. Zhao, J. Tang, K. Pei, et al., "Current-Induced Magnetic Skyrmions With Controllable Polarities in the Helical Phase," *Nano Letters*22 (2022): 8793–8800.

26. D. Song, W. Wang, S. Zhang, et al., "Steady Motion of 80-nm-Size Skyrmions in a 100-nm-Wide Track," *Nature Communications* 15 (2024): 5614.

27. X. Yu, N. Kanazawa, Y. Onose, et al., "Near Room-Temperature Formation of a Skyrmion Crystal in Thin-Films of the Helimagnet FeGe," *Nature Materials* 10 (2011): 106–109.

28. H. Du, X. Zhao, F. N. Rybakov, et al., "Interaction of Individual Skyrmions in a Nanostructured Cubic Chiral Magnet," *Physical Review Letters* 120 (2018): 197203.

29. F. Zheng, F. N. Rybakov, A. B. Borisov, et al., "Experimental Observation of Chiral Magnetic Bobbers in *B*20-Type FeGe," *Nature Nanotechnology* 13 (2018): 451—455.

30. G. P. Müller, F. N. Rybakov, H. J'onsson, S. Blügel, and N. S. Kiselev, "Coupled Quasimonopoles in Chiral Magnets," *Physical Review B* 101 (2020): 184405.

31. A. S. Savchenko, F. Zheng, N. S. Kiselev, et al., "Diversity of States in a Chiral Magnet Nanocylinder," *APL Materials* 10 (2022): 061110.

32. V. M. Kuchkin, N. S. Kiselev, A. Haller, Š. Lišá'ak, A. Michels, and T. L. Schmidt, "Stability and Nucleation of Dipole Strings in Uniaxial Chiral Magnets," *Physical Review B* 111 (2025): 174410.

33. M. Azhar, V. P. Kravchuk, and M. Garst, "Screw Dislocations in Chiral Magnets," *Physical Review Letters* 128 (2022): 157204.

34. F. Zheng, F. N. Rybakov, N. S. Kiselev, et al., "Magnetic Skyrmion Braids," *Nature Communications* 12 (2021): 5316.

35. A. O. Leonov and K. Inoue, "Homogeneous and Heterogeneous Nucleation of Skyrmions in Thin Layers of Cubic Helimagnets," *Physical Review B* 98 (2018): 054404.

36. D. Wolf, S. Schneider, U. K. Rößler, et al., "Unveiling the Three-Dimensional Magnetic Texture of Skyrmion Tubes," *Nature Nanotechnology* 17 (2022): 250–255.

37. J.-S. B. Tai, P. J. Ackerman, and I. I. Smalyukh, "Topological Transformations of Hopf Solitons in Chiral Ferromagnets and Liquid Crystals," *Proceedings of the National Academy of Sciences* 115 (2018): 921–926.

38. P. J. Ackerman and I. I. Smalyukh, "Static Three-Dimensional Topological Solitons in Fluid Chiral Ferromagnets and Colloids," *Nature Materials* 16 (2017): 426–432.

39. F. N. Rybakov, O. Eriksson, and N. S. Kiselev, "Topological Invariants of Vortices, Merons, Skyrmions, and Their Combinations in Continuous and Discrete Systems," *Physical Review B* 111 (2025): 134417.

40. F. N. Rybakov, A. B. Borisov, S. Blügel, and N. S. Kiselev, "New Type of Stable Particlelike States in Chiral Magnets," *Physical Review Letters* 115 (2015): 117201.

41. C. Saji, E. Saavedra, V. L. Carvalho-Santos, A. S. Nunez, and R. E. Troncoso, "Statics and Dynamics of Twisted Skyrmion Tubes in Frustrated Magnets," *Physical Review B* 112 (2025): 134414.

42. V. M. Kuchkin and N. S. Kiselev, "Homotopy Transitions and 3D Magnetic Solitons," *APL Materials* 10 (2022): 071102.

43. P. Midgley and R. E. Dunin-Borkowski, "Electron Tomography and Holography in Materials Science," *Nature Materials* 8 (2009): 271–280.

44. X. Yu, K. V. Iakoubovskii, F. S. Yasin, et al., "Real-Space Observations of Three-Dimensional Antiskyrmions and Skyrmion Strings," *Nano Letters* 22 (2022): 9358–9364.

45. C. Donnelly, M. Guizar-Sicairos, V. Scagnoli, et al., "Three-Dimensional Magnetization Structures Revealed With X-ray Vector Nanotomography," *Nature* 547 (2017): 328–331.

46. F. N. Rybakov and E. Babaev, "Excalibur Software," http://quantumandclassical.com/excalibur/.

47. A. Vansteenkiste, J. Leliaert, M. Dvornik, M. Helsen, F. Garcia-Sanchez, and B. Van Waeyenberge, "The Design and Verification of MuMax3," *AIP Advances* 4 (2014): 107133.

48. A. Hatcher, *Algebraic Topology* (Cambridge Univ. Press, 2002).

49. J. Strom, *Modern Classical Homotopy Theory. Graduate Studies in Mathematics*, vol. 127 (American Mathematical Society, 2011).

50. E. Outerelo and J. M. Ruiz, *Mapping Degree Theory, Graduate Studies in Mathematics*, vol. 108 (AMS Providence, Rhode Island, 2009).

51. B. Berg and M. Lüscher, "Definition and Statistical Distributions of a Topological Number in the Lattice O(3) Sigma-Model," *Nuclear Physics B* 190 (1981): 412.

52. C. Kosniowski, *A First Course in Algebraic Topology* (Cambridge University Press, 1980).

53. A. Marsh, *Mathematics for Physics: An Illustrated Handbook* (World Scientific, 2017).

54. J. J. Rotman, *An Introduction to the Theory of Groups* (Springer-Verlag, NY, 1995).

55. J. Jäykkä and J. Hietarinta, "Unwinding in Hopfion Vortex Bunches," *Physical Review D* 79 (2009): 125027.

56. D. Foster and D. Harland, "Helical Buckling of Skyrme–Faddeev Solitons," *Proceedings of the Royal Society A: Mathematical, Physical and Engineering Sciences* 468 (2012): 3172–3190.

57. R. Knapman, T. Tausendpfund, S. A. Díaz, and K. Everschor-Sitte, "Spacetime Magnetic Hopfions From Internal Excitations and Braiding of Skyrmions," *Communications Physics* 7 (2024): 151.

58. M. Azhar, S. C. Shaju, R. Knapman, A. Pignedoli, and K. Everschor-Sitte, "3D Magnetic Textures With Mixed Topology: Unlocking the Tunable Hopf Index," *arXiv:2411.06929/* (2024).

59. S. C. Shaju, M. Azhar, and K. Everschor-Sitte, "Hopfions in Screw Chiral Magnets," *arXiv:2601.10853/* (2026).

Supporting Information

Additional supporting information can be found online in the Supporting Information section.

Supporting File 1: adma72762-sup-0001-SuppMat.pdf.

Supporting File 2: adma72762-sup-0002-VideoS1.mp4.

Supporting File 3: adma72762-sup-0003-VideoS2.mp4.